Inorganic Chemistry

Article

pubs.acs.org/IC

Raman Spectral and Density Functional Theory Analyses of the CsB_3O_5 Melt Structure

Dexuan Feng,[†] Bo Zhang,[†] Guimei Zheng,[†,‡] Songming Wan,[*,†] and Jinglin You[§]

[†]Anhui Key Laboratory for Photonic Devices and Materials, Anhui Institute of Optics and Fine Mechanics, Chinese Academy of Sciences, Hefei 230031, China

[‡]University of Science and Technology of China, Hefei 230026, China

[§]School of Material Science and Engineering, Shanghai University, Shanghai 200072, China

Supporting Information

ABSTRACT: Melt structures are essential to understand a variety of crystal growth phenomena of alkali-metal triborates, but have not been fully explored. In this work, Raman spectroscopy, coupled with the density functional theory (DFT) method, has been used to solve the CsB_3O_5 (CBO) melt structure. When the CBO crystal melts, the extra-ring B_4−Ø bonds (the B−Ø bonds of $BØ_4$ groups, Ø = bridging oxygen atom) that connect two $B_3O_3Ø_4$ rings (the basic boron−oxygen unit in the CBO crystal structure) break. As a result, the three-dimensional boron−oxygen network collapses to unique polymer-like $[B_3O_4Ø_2]_n$ chains. On the basis of the optimized $[B_3O_4Ø_2]_n$ chain model, the CBO melt Raman spectrum was calculated by the DFT method for the first time and the calculated results confirm that the $[B_3O_4Ø_2]_n$ chain is the primary species in the CBO melt. These results also demonstrate the capability of the combined Raman spectral and DFT method for analyzing borate melt structures.

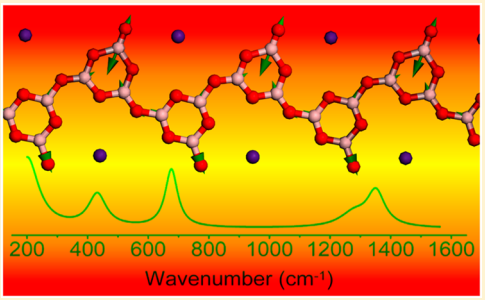

INTRODUCTION

Nonlinear optical (NLO) crystals are widely used to produce coherent light at new wavelengths. Alkali-metal triborates LiB_3O_5 (LBO), CsB_3O_5 (CBO), and $CsLiB_6O_{10}$ (CLBO) are excellent NLO crystals characterized by moderate NLO coefficients, high transparency in the visible and UV regions, and high resistance against laser-induced damage.[1,2] LBO is the first alkali-metal triborate crystal reported for NLO applications.[3] Over the last two decades, LBO has become the most widely used NLO crystal for the second- and third-harmonic generations (SHG and THG) of Nd:YAG lasers. CBO as compared to LBO possesses superior THG performance and can be employed to generate a 185 nm UV laser, which cannot be realized by most NLO crystals.[4,5] CLBO distinguishes itself from other NLO crystals by its outstanding abilities for generating the fourth and the fifth harmonics of Nd:YAG lasers[6,7] and has been employed in several commercial solid-state UV laser systems. In addition, because of the high laser damage thresholds, the three crystals are also promising candidates for use in high-power lasers, such as the inertial confinement fusion laser and the sodium guide star laser.[8−10]

Efficient and reliable lasers, especially those of high power, depend greatly on high-quality and large-sized crystals. LBO, CBO, and CLBO crystals are often grown from high-temperature melts (or solutions).[11−13] The melt structures are related not only to the crystal growth microprocesses (mechanism, phase transition, etc.) but also to the melt macroproperties (viscosity, volatility, surface tension, etc.). Knowledge of the melt structures can help us to deeply understand the crystal growth phenomena, to further improve the crystal growth techniques, and finally to obtain high-quality and large-sized crystals.[14] However, in spite of the theoretical and technological importance, the knowledge of the alkali-metal triborate melt structures is still very limited.

The LBO, CBO, and CLBO melts can be obtained by melting the corresponding crystals. Since the LBO, CBO, and CLBO crystal structures have been determined, if the crystal-to-melt structural transformations are fully understood, the LBO, CBO, and CLBO melt structures will be deduced.

LBO, CBO, and CLBO crystals are all built up of triborate groups ($B_3O_3Ø_4$, Ø = bridging oxygen atom) together with alkali-metal cations.[15−17] More interestingly, the three crystals melt at almost the same temperature (the melting points of LBO, CBO, and CLBO are 834, 835, and 848 °C, respectively[18−20]), which implies that the three crystals probably undergo a similar structural transformation in the melting processes, and thus the resultant LBO, CBO, and CLBO melts probably have similar structures. In a previous work, we have studied the structural transformation near a CBO crystal−melt interface by high-temperature Raman spectroscopy. An isomerization reaction between 3- and 4-coordinated boron atoms was discovered in this region.[21] Three years later, Hou et al. found the same isomerization reaction in a CBO crystal melting process.[22] According to the structural transformation, they deemed that the CBO melt structure was

Received: April 24, 2016
Published: July 1, 2016

DOI: 10.1021/acs.inorgchem.6b01020
Inorg. Chem. 2016, 55, 7098−7102

made up of Cs^+ cations and polymer-like boron−oxygen chains whose basic unit was the $B_3O_4Ø_2$ group. Then the Hartree−Fock (HF) theoretical method was employed to calculate the melt Raman spectrum with the $CsH_2B_3O_6$ isolated group as the structural model (the two bridging oxygen atoms of the $CsB_3O_4Ø_2$ group are saturated with two hydrogen atoms). Unfortunately, the calculated Raman spectrum did not agree very well with the experimental one. The disagreement is largely due to the deficiencies of the HF theoretical method and the crude approximation of the H-terminated structural model.[23] In order to settle the problems and further to determine the CBO melt structure, a more accurate theoretical method and a more accurate structural model are necessary.

The density functional theory (DFT) method is a powerful tool for calculating crystal Raman spectra.[24] Recently, the method has been developed to analyze high-temperature Raman spectra with the aim to solve melt structures.[25−27] In this work, the DFT method was used to investigate the CBO crystal Raman spectrum and then to analyze the crystal-to-melt structural transformation. The unique $[B_3O_4Ø_2]_n$ chain was inferred to be the primary species in the CBO melt and confirmed by the DFT method for the first time.

EXPERIMENTAL SECTION

Instrumentation. The experimental system has been described elsewhere.[21,28] It consists of a homemade microfurnace and a commercial high-temperature confocal Raman spectrometer (Jobin Y'von LabRam HR800). The microfurnace is made up of a water jacket surrounding a main sample chamber. An alumina heating base, which provides a horizontal temperature gradient across a platinum boat, is placed in the center of the sample chamber. The spatial resolution and accumulated time resolution techniques are adopted in the spectrometer in order to improve the signal-to-noise ratio.[29] The 532 nm line of a Q-switched pulsed SHG-Nd:YAG laser is employed as the excitation source, and an intensive charge couple device (ICCD) as the detector.

Sample Preparation and Raman Spectroscopic Measurements. A CBO boule was cut into slices with a size of 2 × 5 × 10 mm^3. One such slice was placed into the platinum boat and then heated by the microfurnace. The heating rate was carefully controlled to ensure that the crystal melted at the temperature just above its melting point. The crystal/melt Raman spectra were collected with a back-scattering configuration. The average power of the excitation source was fixed at 800 mW. The spectra were recorded in an accumulated mode with 100 s integration time. The spectral range of interest is from 200 to 1800 cm^{-1} with a spectral resolution of 2 cm^{-1}.

DFT Calculation. The CBO crystal structure, which was determined by single-crystal X-ray diffraction,[16] was adopted as the initial model for the crystal Raman spectrum analysis. A CBO melt structure, which was inferred on the bases of the CBO crystal structure and the crystal-to-melt structural transformation, was adopted as the initial structural model for the melt Raman spectrum analysis. All of the DFT calculations were performed by the plane-wave pseudopotential method implemented in the Cambridge sequential total energy package (CASTEP) code.[30,31] Exchange and correlation energies were described by the Wu−Cohen (WC) functional of the generalized gradient approximation (GGA).[32] The total energy convergence tolerance was 5 × 10^{-6} eV/atom with a self-consistent-field (SCF) convergence criterion of 5 × 10^{-7} eV/atom, a maximum force tolerance of 0.01 eV/Å, and a maximum displacement of 5 × 10^{-4} Å. Plane-wave cutoff energies and Γ-centered *k*-point grids have been tested in order to converge the total energies. According to the test results (see the Supporting Information Table S1, Figure S1, Table S2, and Figure S2 for more details), a cutoff energy of 1100 eV and a *k*-space grid of 2 × 2 × 2 were used for the crystal calculation, and a cutoff energy of 1000 eV and a *k*-space grid of 2 × 2 × 3 for the melt calculation.

The initial structural models were optimized in order to obtain the energy minima. On the basis of the optimized structures, the Raman frequencies were obtained by diagonalization of dynamical matrices computed by density functional perturbation theory (DFPT),[33] and the Raman intensities were calculated using a hybrid DFPT and finite displacements method.[34] All of the calculated Raman intensities were corrected by the Bose−Einstein population factors with the exciting wavelength (532 nm) and the experimental temperatures (300 K for the crystal and 1110 K for the melt).[35] Then, the Raman spectra were fitted with Gaussian line shape functions by the SWizard software.[36]

RESULTS AND DISCUSSION

CBO crystallizes in the orthorhombic $P2_12_12_1$ space group with a = 6.213 Å, b = 8.521 Å, c = 9.170 Å, and Z = 4. Its structure is built up of identical $B_3O_3Ø_4$ six-membered rings that are connected with each other to form a three-dimensional boron−oxygen network. Cs^+ cations are located at the interstices of the network.[16] Upon melting, the CBO crystal structure will transform to the CBO melt structure. In the present study, the structural transformation is reflected by the Raman spectral change. In order to understand the structural origin of the spectral change, the crystal Raman spectrum should be accurately analyzed.

Several experimental and theoretical studies have been made on the CBO crystal Raman spectrum.[22,37] However, in view of the structural complexity of the $B_3O_3Ø_4$ ring, the Raman bands were approximately attributed to the vibrations of a B_3O_6 ring and a $BØ_4$ tetrahedron, although the two groups are quite different from the $B_3O_3Ø_4$ ring. In order to provide more accurate assignments of some important Raman bands, the CBO crystal Raman spectrum was reinvestigated herein by the DFT method.

The experimental and calculated Raman spectra are shown in Figure 1. It can be seen from the figure that the calculated

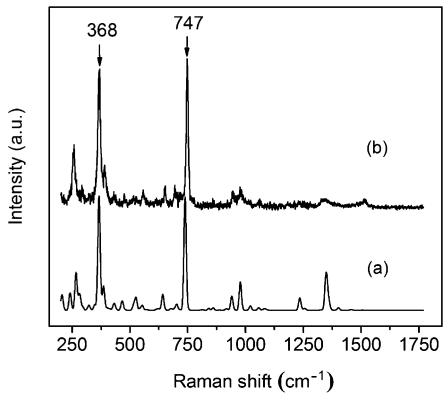

Figure 1. (a) Calculated and (b) experimental Raman spectra of the CBO crystal.

spectrum coincides with the experimental one, which indicates that the DFT method is reliable for analyzing the Raman spectra of the cesium−boron−oxygen system. According to the calculated results, all the Raman bands are assigned (see the Supporting Information Table S3 for more details). Figure 2 gives the atomic displacements corresponding to the two strongest bands in the CBO crystal Raman spectrum. The 368 cm^{-1} (experimental value) band is mainly related to the bending vibration of the $BØ_4$ group in the $B_3O_3Ø_4$ ring, and the 747 cm^{-1} (experimental value) band is related to the breathing vibration of the $B_3O_3Ø_4$ ring.

DOI: 10.1021/acs.inorgchem.6b01020
Inorg. Chem. 2016, 55, 7098−7102

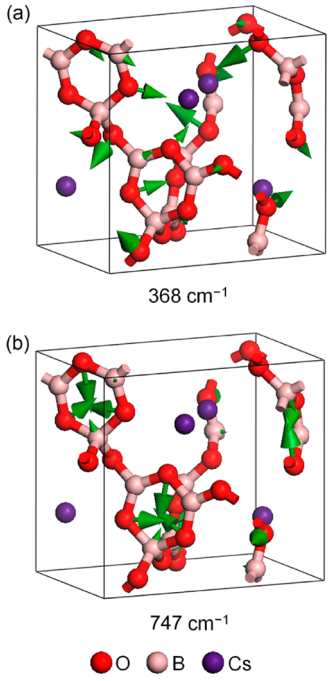

Figure 2. Atomic displacements of two strongest bands in the CBO crystal Raman spectrum: (a) the 368 cm^{-1} band and (b) the 747 cm^{-1} band.

The CBO melt Raman spectrum was recorded near its freezing point. It has three strong vibrational bands located in the ranges of 360−580, 600−1000, and 1200−1600 cm^{-1}, as shown in Figure 3. After melting, (1) the crystal 368 cm^{-1} band

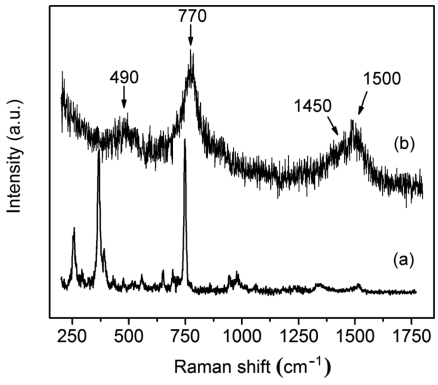

Figure 3. Raman spectra of (a) the CBO crystal at room temperature and (b) the CBO melt near its freezing point.

disappears. According to the DFT-calculated results, the band mainly arises from the bending vibration of the $BØ_4$ group in the $B_3O_3Ø_4$ ring, and thus the band disappearance indicates that the $BØ_4$ group vanishes in the melting process. (2) The crystal 747 cm^{-1} band shifts to around 770 cm^{-1} slightly but anomalously. The DFT-calculated results show that the 747 cm^{-1} band is attributed to the breathing vibration of the $B_3O_3Ø_4$ ring. Thus, the slight shift implies that a similarly structured boron−oxygen ring is present in the melt, and the anomalous blue shift implies that its structure is different from the $B_3O_3Ø_4$ ring. (3) A new strong band appears in the range of 1200−1600 cm^{-1}. Raman bands in this range are generally assigned to the stretching vibrations of the extra-ring B−O bond/bonds of a boron−oxygen six-membered ring.[26,38] Therefore, the band appearance suggests that a new boron−oxygen six-membered ring with the extra-ring B−O bond/bonds is present in the CBO melt.

All of the above analyses reveal that, when the CBO crystal melts, the extra-ring B_4−Ø bonds (the B−Ø bonds of $BØ_4$ groups) that connect two $B_3O_3Ø_4$ rings break, and as a result, all of the $B_3O_3Ø_4$ rings transform to the $B_3O_4Ø_2$ rings, as shown in Figure 4. To the best of our knowledge, the $B_3O_4Ø_2$ ring is a unique boron−oxygen ring that has not been found in crystalline borate compounds.[39]

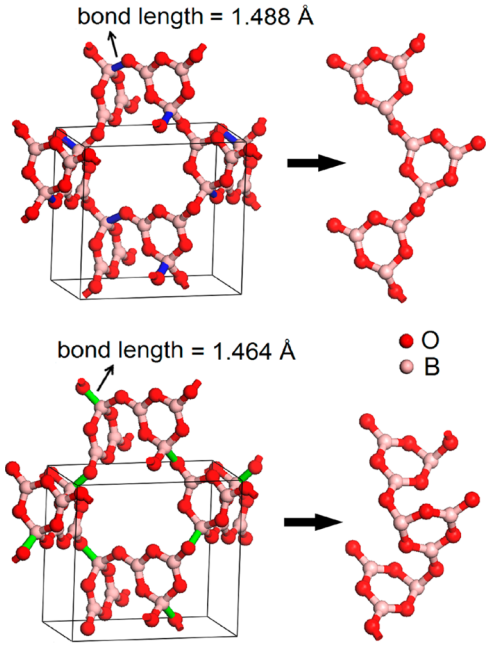

Figure 4. Two possible structural transformations from the $B_3O_3Ø_4$ crystal network to the $[B_3O_4Ø_2]_n$ melt chains.

Every $B_3O_3Ø_4$ ring in the CBO crystal includes two types of extra-ring B_4−Ø bonds whose lengths are 1.488 and 1.464 Å (see Figure 4).[16] Thus, when the B_4−Ø bonds break, the CBO crystal can collapse to two types of polymer-like $[B_3O_4Ø_2]_n$ chains with different spatial arrangements (Figures 4 and 5). The two types of chains inherit the structural periodicity of the crystal, and every period includes two $B_3O_4Ø_2$ rings. We deem that these chains will further transform to more stable spatial arrangements in the melt. In order to determine the stable spatial arrangements, the two types of chains (Figure 5a and b)

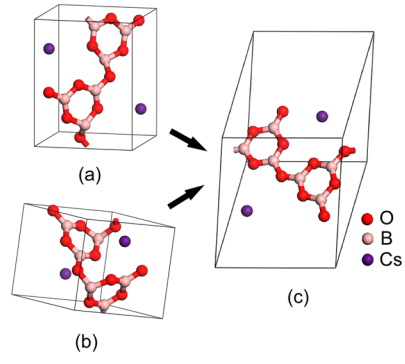

Figure 5. Initial and optimized CBO melt structural models: (a) the initial model 1; (b) the initial model 2; and (c) the optimized model.

DOI: 10.1021/acs.inorgchem.6b01020
Inorg. Chem. 2016, 55, 7098−7102

were structurally optimized by the DFT method. Two neighboring $B_3O_4Ø_2$ rings were placed into a unit cell with two Cs^+ cations to balance the charge of the groups (see Figure 5; more structural details are supplied in the Supporting Information Figure S3, Table S4, Figure S4, and Table S5). Considering the strong electrostatic interaction between the chains and the Cs^+ cations, the structural optimization was performed without limitation of the unit cell parameters and the atomic positions. Interestingly, the two optimized chains have an identical spatial arrangement (see Figure 5c; more structural details are supplied in the Supporting Information Figure S5 and Table S6). As compared with the initial structures, the optimized melt structure has the same constituent group ($B_3O_4Ø_2$ ring), but a different molecular conformation.

The CBO melt Raman spectrum was calculated by the DFT method on the basis of the optimized structural model. The calculated Raman bands were broadened by Gaussian line shape functions. Considering that different vibrational modes have different full widths at half-maximum (FWHM's), we employed the experimental FWHM's (the FWHM values of the experimental bands located in the ranges of 200−600, 600−1200, and 1200−1800 cm^{-1} are 120, 60, and 120 cm^{-1}, respectively) to broaden the calculated Raman bands. For comparison, the calculated spectrum was also broadened by the Gaussian line shape function with a FWHM of 1 cm^{-1}. The calculated spectra, together with the experimental spectrum, are shown in Figure 6. It can be seen from the figure that the calculated Raman spectrum (Figure 6b) is in agreement with the experimental one (Figure 6c), which proves that the structural model shown in Figure 5c can be used to describe the CBO melt structure.

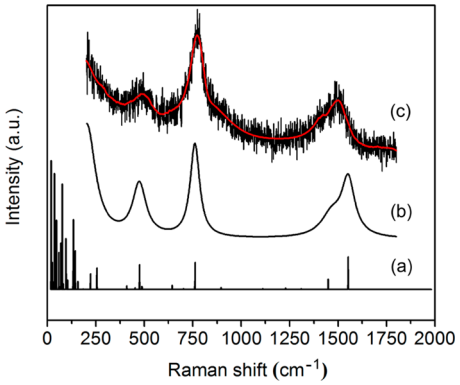

Figure 6. Calculated CBO melt Raman spectra broadened by Gaussian line shape functions (a) with a FWHM of 1 cm^{-1} and (b) with the experimental FWHM; (c) the experimental CBO melt Raman spectrum.

Previous works have showed that the melt Raman spectra of LBO and CLBO are very close to that of CBO,[40,41] which suggests that the LBO and CLBO melts are also made up of the $[B_3O_4Ø_2]_n$ chains.

The calculation also provides accurate assignments for all of the vibrational bands in the CBO melt Raman spectrum. The band located around 490 cm^{-1} (experimental value) mainly arises from the wagging vibration of the $B_3O_4Ø_2$ rings; the 770 cm^{-1} (experimental value) strong band is related to the breathing vibration of the $B_3O_4Ø_2$ rings; the shoulder band located around 1450 cm^{-1} (experimental value) originates from the stretching vibration of the intra-ring B−O bonds; and the strong band located around 1500 cm^{-1} (experimental value) is attributed to the stretching vibration of the extra-ring B−O bonds. The atomic displacements of the four main bands are shown in Figure 7. The assignments of the other vibrational modes are listed in the Supporting Information Table S7.

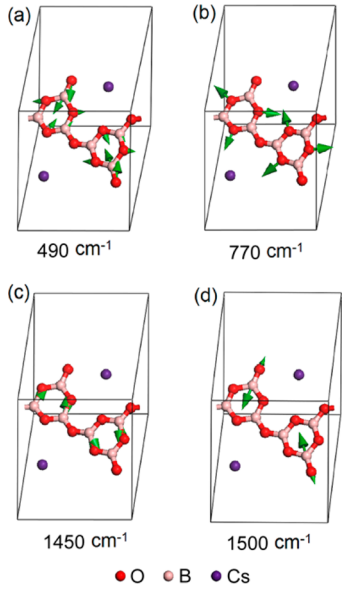

Figure 7. Atomic displacements of the four main bands in the CBO melt spectrum. (a) The 490 cm^{-1} (experimental value, the same as below) band, (b) the 770 cm^{-1} band, (c) the 1450 cm^{-1} band, and (d) the 1500 cm^{-1} band.

CONCLUSIONS

When the CBO crystal melts, the extra-ring B_4−Ø bonds that connect two $B_3O_3Ø_4$ rings break, and as a result, the three-dimensional boron−oxygen network collapses to unique polymer-like $[B_3O_4Ø_2]_n$ chains. The DFT results further show that the $[B_3O_4Ø_2]_n$ chains have a fixed spatial arrangement in the melt. The calculated CBO melt Raman spectrum based on the optimized $[B_3O_4Ø_2]_n$ chain model is consistent with the experimental one, confirming that the CBO melt is made up of the $[B_3O_4Ø_2]_n$ chains and Cs^+ cations. The calculation also provides accurate assignments for the main vibrational bands present in the CBO melt spectrum.

The work verifies that the DFT method, combined with high-temperature Raman spectroscopy, is a reliable tool to analyze the CBO melt structure and Raman spectrum. The $[B_3O_4Ø_2]_n$ chain structure provides a new standpoint for deeply understanding the microprocess of the CBO crystal growth and the macroproperties of the CBO melt, which can help us to better interpret the crystal growth phenomena of CBO and other alkali-metal triborates such as LBO and CLBO.

ASSOCIATED CONTENT

Supporting Information

The Supporting Information is available free of charge on the ACS Publications website at DOI: 10.1021/acs.inorgchem.6b01020.

Convergence tests for the CBO crystal and the CBO melt total energies with respect to the Γ-centered *k*-point grids and the cutoff energies, calculated CBO crystal

DOI: 10.1021/acs.inorgchem.6b01020
Inorg. Chem. 2016, 55, 7098−7102

vibrational modes and their frequencies, the initial CBO melt structural models and their geometrical parameters, the optimized CBO melt structural model and its geometrical parameters, and calculated CBO melt vibrational modes and their frequencies (PDF)

AUTHOR INFORMATION

Corresponding Author

*E-mail (S. Wan): smwan@aiofm.ac.cn.

Notes

The authors declare no competing financial interest.

ACKNOWLEDGMENTS

The work is financially supported by the National Natural Science Foundation of China (Grant No. 51372246). The calculations were partially performed at the Center for Computational Science, CASHIPS.

REFERENCES

(1) Chen, C. T.; Sasaki, T.; Li, R. K.; Wu, Y. C.; Lin, Z. S.; Mori, Y.; Hu, Z. G.; Wang, J. Y.; Aka, G.; Yoshimura, M.; Kaneda, Y. *Nonlinear Optical Borate Crystals: Principles and Applications*; Wiley-VCH Verlag GmbH & Co. KGaA: Weinheim, Germany, 2012.

(2) Becker, P. *Adv. Mater.* **1998**, *13*, 979−992.

(3) Chen, C. T.; Wu, Y. C.; Jiang, A. D.; Wu, B. C.; You, G. M.; Li, R. K.; Lin, S. J. *J. Opt. Soc. Am. B* **1989**, *6*, 616−621.

(4) Wu, Y. C.; Fu, P. Z.; Wang, J. X.; Xu, Z. Y.; Zhang, L.; Kong, Y. F.; Chen, C. T. *Opt. Lett.* **1997**, *22*, 1840−1842.

(5) Kitano, H.; Matsui, T.; Sato, K.; Ushiyama, N.; Yoshimura, M.; Mori, Y.; Sasaki, T. *Opt. Lett.* **2003**, *28*, 263−265.

(6) Mori, Y.; Kuroda, I.; Nakajima, S.; Sasaki, T.; Nakai, S. *Appl. Phys. Lett.* **1995**, *67*, 1818−1820.

(7) Wang, G. L.; Geng, A. C.; Bo, Y.; Li, H. Q.; Sun, Z. P.; Bi, Y.; Cui, D. F.; Xu, Z. Y.; Yuan, X.; Wang, X. Q.; Shen, G. Q.; Shen, D. Z. *Opt. Commun.* **2006**, *259*, 820−822.

(8) Yap, Y. K.; Haramura, S.; Taguchi, A.; Mori, Y.; Sasaki, T. *Opt. Commun.* **1998**, *145*, 101−104.

(9) Hiromitsu, K.; Norihiro, I.; Koichi, Y. *Opt. Express* **2002**, *10*, 1028−1032.

(10) Denman, C. A.; Hillman, P. D.; Moore, G. T.; Telle, J. M.; Preston, J. E.; Drummond, J. D.; Fugate, R. Q. *Proc. SPIE* **2005**, *5707*, 46−49.

(11) Zhao, S. Q.; Huang, C. E.; Zhang, H. W. *J. Cryst. Growth* **1990**, *99*, 805−810.

(12) Fu, P. Z.; Wang, J. X.; Hu, Z. G.; Wu, Y. C.; Yin, S. T.; Xu, Z. Y. *J. Synth. Cryst.* **1999**, *28*, 215−218 (in Chinese).

(13) Mori, Y.; Kuroda, I.; Nakajima, S.; Taguchi, A.; Sasaki, T.; Nakai, S. *J. Cryst. Growth* **1995**, *156*, 307−309.

(14) Ginkin, V.; Kartavykh, A.; Zabudko, M. *J. Cryst. Growth* **2004**, *270*, 329−339.

(15) Konig, H.; Hoppe, R. *Z. Anorg. Allg. Chem.* **1978**, *439*, 71−79.

(16) Krogh-Moe, J. *Acta Crystallogr., Sect. B: Struct. Crystallogr. Cryst. Chem.* **1974**, *30*, 1178−1180.

(17) Sasaki, T.; Mori, Y.; Kuroda, I.; Nakajima, S.; Yamaguchi, K.; Watanabe, S.; Nakai, S. *Acta Crystallogr., Sect. C: Cryst. Struct. Commun.* **1995**, *51*, 2222−2224.

(18) Sastry, B. S. R.; Hummel, F. A. *J. Am. Ceram. Soc.* **1958**, *41*, 7−17.

(19) Penin, N.; Touboul, M.; Nowogrocki, G. *J. Cryst. Growth* **2003**, *256*, 334−340.

(20) Mori, Y.; Kuroda, I.; Nakajima, S.; Taguchi, A.; Sasaki, T.; Nakai, S. *J. Cryst. Growth* **1995**, *156*, 307−309.

(21) Wan, S. M.; Zhang, X.; Zhao, S. J.; Zhang, Q. L.; You, J. L.; Lu, L.; Fu, P. Z.; Wu, Y. C.; Yin, S. T. *Cryst. Growth Des.* **2008**, *8*, 412−414.

(22) Hou, M.; You, J. L.; Patrick, S.; Zhang, G. C.; Wan, S. M.; Wang, Y. Y.; Ji, Z. F.; Wang, L. H.; Fu, P. Z.; Wu, Y. C.; Yin, S. T. *CrystEngComm* **2011**, *13*, 3030−3034.

(23) DeFrees, D. J.; McLean, A. D. *J. Chem. Phys.* **1985**, *82*, 333−341.

(24) Milman, V.; Refson, K.; Clark, S. J.; Pickard, C. J.; Yates, J. R.; Gao, S. P.; Hasnip, P. J.; Probert, M. I. J.; Perlov, A.; Segall, M. D. *J. Mol. Struct.: THEOCHEM* **2010**, *954*, 22−35.

(25) Sun, Y. L.; Wan, S. M.; Lv, X. S.; Tang, X. L.; You, J. L.; Yin, S. T. *CrystEngComm* **2013**, *15*, 995−1000.

(26) Wan, S. M.; Tang, X. L.; Sun, Y. L.; Zhang, G. C.; You, J. L.; Fu, P. Z. *CrystEngComm* **2014**, *16*, 3086−3090.

(27) Wan, S. M.; Zhang, B.; Sun, Y. L.; Tang, X. L.; You, J. L. *CrystEngComm* **2015**, *17*, 2636−2641.

(28) Wan, S. M.; Zhang, X.; Zhao, S. J.; Zhang, Q. L.; You, J. L.; Chen, H.; Zhang, G. C.; Yin, S. T. *J. Appl. Crystallogr.* **2007**, *40*, 725−729.

(29) You, J. L.; Jiang, G. C.; Chen, H.; Wu, Y. Q.; Xu, K. D.; Zhang, S. L. In *Synopsis of International Conference on Raman Spectroscopy*; Gold Coast, Australia, August 8−13, 2004; pp 224−225.

(30) Segall, M. D.; Lindan, P. J. D.; Probert, M. J.; Pickard, C. J.; Hasnip, P. J.; Clark, S. J.; Payne, M. C. *J. Phys.: Condens. Matter* **2002**, *14*, 2717−2744.

(31) Baroni, S.; de Gironcoli, S.; Dal Corso, A.; Giannozzi, P. *Rev. Mod. Phys.* **2001**, *73*, 515−562.

(32) Wu, Z. G.; Cohen, R. E. *Phys. Rev. B: Condens. Matter Mater. Phys.* **2006**, *73*, 235116.

(33) Refson, K.; Clark, S. J.; Tulip, P. R. *Phys. Rev. B: Condens. Matter Mater. Phys.* **2006**, *73*, 155114.

(34) Porezag, D.; Pederson, M. R. *Phys. Rev. B: Condens. Matter Mater. Phys.* **1996**, *54*, 7830−7836.

(35) Yano, T.; Kunimine, N.; Shibata, S.; Yamane, M. *J. Non-Cryst. Solids* **2003**, *321*, 137−168.

(36) Gorelsky, S. I.; Lever, A. B. P. *J. Organomet. Chem.* **2001**, *635*, 187−196.

(37) Wang, Y. F.; Liu, J. J.; Hu, S. F.; Lan, G. X.; Fu, P. Z.; Wang, Z. X. *J. Raman Spectrosc.* **1999**, *30*, 519−523.

(38) Kamitsos, E. I.; Karakassides, M. A.; Chryssikos, G. D. *Phys. Chem. Glasses* **1989**, *30*, 229−234.

(39) Heller, G. *Top. Curr. Chem.* **1986**, *131*, 39−98.

(40) Feng, D. X.; Zheng, G. M.; Zhao, Y.; Zhang, B.; Wan, S. M.; You, J. L.; Hu, Z. G. *CrystEngComm* **2015**, *17*, 9357−9362.

(41) Wang, J.; You, J. L.; Wang, Y. Y.; Zhang, G. C.; Wan, S. M.; Fu, P. Z.; Yin, S. T.; Liu, Q.; Wang, C. Y.; Liu, X. W. *J. Synth. Cryst.* **2013**, *42*, 397−401 (in Chinese).

DOI: 10.1021/acs.inorgchem.6b01020
Inorg. Chem. 2016, 55, 7098−7102